Dragonfly – Aerodynamics during Transition to Powered Flight

Jason Cornelius, Tomas Opazo
Sven Schmitz, and Jack Langelaan
Dept. of Aerospace Engineering
The Pennsylvania State University
University Park, PA, USA

Benjamin Villac, Douglas Adams
and Lev Rodovskiy
Johns Hopkins APL
Applied Physics Laboratory
Laurel, MD, USA

Larry Young
Aerospace Engineer
Aeromechanics Office
NASA Ames Research Center
Moffett Field, CA, USA

ABSTRACT

The Dragonfly lander will enter the Titan atmosphere following an approximate 7–10-year journey through space inside its aeroshell. After atmospheric entry, deployment of the main parachute, and heatshield release, the lander will begin its transition to powered flight (TPF). TPF is a maneuver sequence used for mid-air deployment of the Dragonfly rotorcraft lander. The sequence starts just after lander release with the rotors lightly loaded and finishes when a steady-state descent condition has been attained. Mid-air deployment of a multicopter unmanned aerial system is a multi-disciplinary problem involving controller choice and tuning, trajectory planning and optimization, and computational fluid dynamics analyses. This paper is an introduction to the transition of rotor flow states in TPF from the windmill brake state, through the turbulent wake state and vortex ring state, and the successful emergence into a normal operating state. A particle swarm optimized controller's nominal trajectory is plotted on a rotor aerodynamics state chart to show the trajectory's path through the flow states along the TPF maneuver. Results of preliminary CFD simulations show the variance of individual rotor thrust and power in the early stages of TPF followed by a successful stabilization of rotor performance. Interactional aerodynamic studies also characterize the pre-release flowfield around the lander to be benign at the start of the maneuver. Additionally, results for the lander in steady axial descent show a previously observed coaxial rotor shielding phenomenon of the upper rotor from the effects of vortex ring state.

NOTATION

CAD	Computer Aided Design
CFD	Computational Fluid Dynamics
ESC	Electronic Speed Controller
NACA	National Advisory Committee for Aeronautics
P	Rotor Power [W]
Phase A	Concept Study Model
PID	Proportional-Integral-Derivative
PSO	Particle Swarm Optimization
P_{atm}	Atmospheric Reference Pressure [Pa]
RANS	Reynolds-Averaged Navier-Stokes
RotCFD	Rotorcraft Computational Fluid Dynamics
RPM	Revolutions per Minute
T	Rotor Thrust [N]
TPF	Transition to Powered Flight
TWS	Turbulent Wake State
URANS	Unsteady Reynolds Averaged Navier-Stokes
VRS	Vortex Ring State
VTOL	Vertical Take-Off and Landing
V_x	Rotor Edgewise (Forward) Speed [m/s]
V_z	Rotor Axial (Vertical) Speed [m/s]
v_h	Equivalent Hover Induced Velocity [m/s]
v	Rotor Induced Velocity [m/s]
WBS	Windmill Brake State
α	Rotor Angle of Attack [deg]
ρ	Density [kg/m^3]
μ	Dynamic Viscosity [kg/m-s]

INTRODUCTION

Saturn's largest moon Titan is a unique cryogenic (90 K, -183 C) world in the solar system. It is larger than Mercury, yet has lower gravity than Earth's Moon, and presents a unique thick nitrogen atmosphere that supports weather cycles and pre-biotic chemistry [1]. In many ways, Titan is very Earth-like with respect to the early days of our home planet, i.e. prior to the origin of life as we know it. The Cassini mission and its Huygens probe have vastly furthered our understanding of Titan, but one of the remaining questions yet to be answered is regarding its surface composition. In particular, it is unknown today how far the organic rich surface composition on Titan has ascended up the "ladder of life." Closing this knowledge gap will potentially advance the understanding of the origin of life here on Earth. Titan's topography is a highly variable landscape with plains and dune fields much like in desert regions on Earth; its low gravity (about that of our Moon) and thick atmosphere (about four times denser than sea-level on Earth) make Titan feasible for aerial exploration in general and in particular for vertical flight concepts [2-8]. Table 1 shows the comparison of atmospheric properties between Earth and Titan.

Presented at the Vertical Flight Society's 77th Annual Forum & Technology Display, Virtual, May 10-14, 2021.

Table 1. Atmospheric Conditions on Titan and Earth

Atmospheric Variable	Titan	Earth	Titan/ Earth
Density, ρ (kg/m^3)	5.4	1.225	4.41
Dynamic Viscosity, μ $(kg/m-s)$	$6.7x10^{-6}$	$1.8x10^{-5}$	0.37
Reference Pressure, P_{atm} (Pa)	146,086	101,325	1.44
Speed of Sound, a (m/s)	195	343	0.57
Gravitational Acceleration, g (m/s^2)	1.35	9.81	0.14

In June 2019, NASA selected Dragonfly as the 4th New Frontiers Mission. Dragonfly is designed as a relocatable lander, more specifically as an octocopter consisting of four pairs of coaxial rotors arranged in an X8 configuration attached to a central lander body [9]. Dragonfly is expected to launch late in the 2020s and arrive at Titan in the mid-2030s. While on Titan, Dragonfly will perform dozens of flights over a period of more than three years. Dragonfly will be the first vertical take-off and landing (VTOL) vehicle sent to another world for sustained exploration, and will be capable of traversing more than a hundred kilometers [10].

Although Dragonfly will be the first VTOL vehicle with an extended exploration mission, the first VTOL vehicle to take flight on another planetary body was the technology demonstrator Ingenuity, which first flew on Mars on April 19th, 2021 [11-12]. Several trade studies have been carried out to characterize the feasibility of flight on both Mars and Titan and other planetary bodies since the early 2000s [13-16]. Studies have more recently focused on preparing proposals for NASA science missions such as the Aerial Vehicle for in-situ and Airborne Titan Reconnaissance (AVIATR) and the Titan Mare Explorer (TiME) conceptual designs for exploration of Titan [17-18].

The Dragonfly mission is continuing down this path and has already undergone a great deal of developmental work. This paper will focus on the rotor aerodynamics associated with what the program terms Transition to Powered Flight (TPF). Additionally, an early controller approach will be briefly discussed at a high level to give the reader a broad overview of a notional rotor control system and its operation during TPF. Interactional aerodynamic analyses of the aeroshell under parachute descent pre- and post-heatshield and lander release will also be shown. Results of the lander in steady axial descent will also be discussed and qualitatively compared to the relevant segments of TPF. The results presented in this paper are based on the concept study model (Phase A) and aim to demonstrate the tools and approach used in the analysis of the TPF maneuver.

DRAGONFLY – TITAN ARRIVAL & TRANSITION TO POWERED FLIGHT (TPF)

After an approximate 7–10-year journey through the solar system, Dragonfly will perform a ballistic entry into Titan's atmosphere followed by a drogue chute deployment. After an extended descent on the drogue chute, the main parachute will be deployed in the lower atmosphere and the heatshield will be jettisoned from the backshell (Fig. 1, left). Following a despin procedure, the lander will be released from the backshell (Fig. 2), and Dragonfly will initiate the TPF maneuver away from the backshell and parachute. The lander will then transition into a steady-descent forward-flight condition in order to land on Titan's surface (Fig. 1, right).

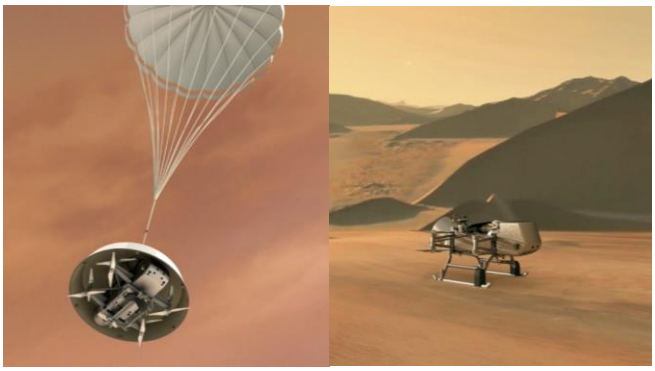

Figure 1. Heatshield Jettisoned (left), Lander on Titan (right), Pictures Courtesy of Dragonfly/JHUAPL

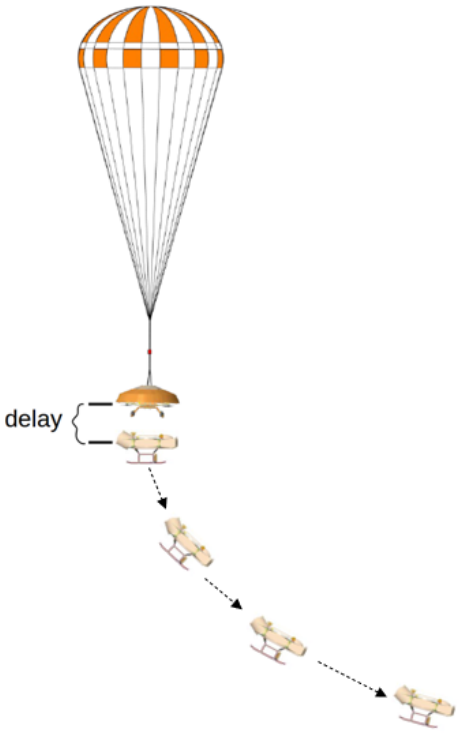

Figure 2. Transition to Powered Flight Maneuver

Dragonfly begins the TPF maneuver after atmospheric entry and descent by first going into a one second free-fall (delay) to create positive separation from the backshell. A pitch-forward maneuver is then conducted to reduce the rotor angle of attack α, and start the lander on a trajectory away from the backshell. The lander then uses its onboard control system to track a prescribed descent profile to a few hundred meters above the ground. Dragonfly will search the planned landing area with cameras and other sensors to determine a suitable location for the first touchdown.

Figure 3 shows a notional schematic of lander attitudes and velocities during the TPF maneuver and Fig. 4 shows the rotor and lander coordinate system definitions [19]. The first step of the maneuver involves successfully passing through the windmill brake state (WBS – Fig. 3, pt. 0), turbulent wake state (TWS – Fig. 3, pt. 1), and vortex ring state (VRS – Fig. 3, pt. 2), which is a challenge for mid-air deployment of any multicopter vehicle. This mid-air deployment problem and what it means for the rotor aerodynamics will now be discussed.

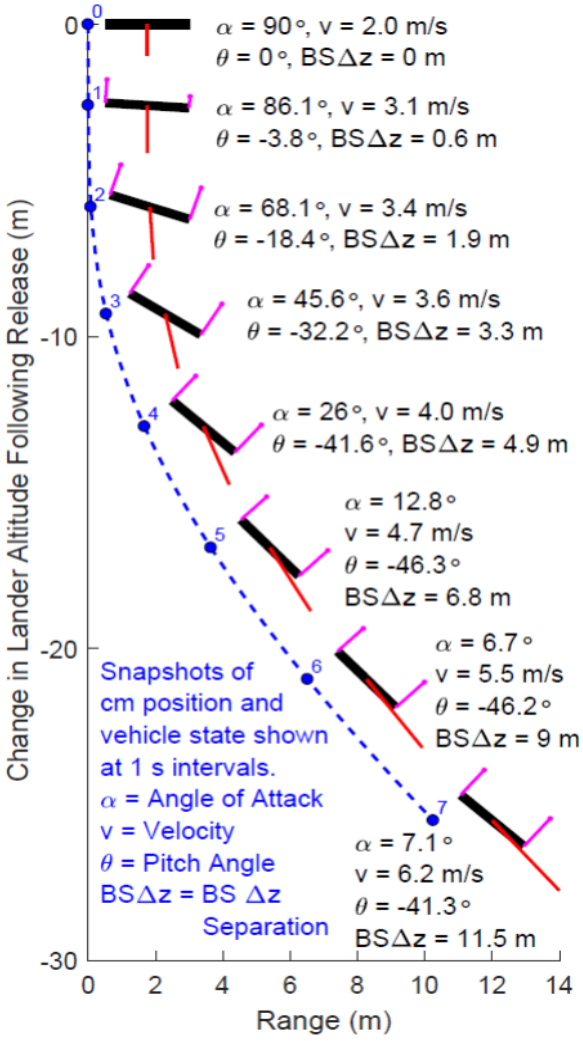

Figure 3. Notional Phase A TPF Profile [19]

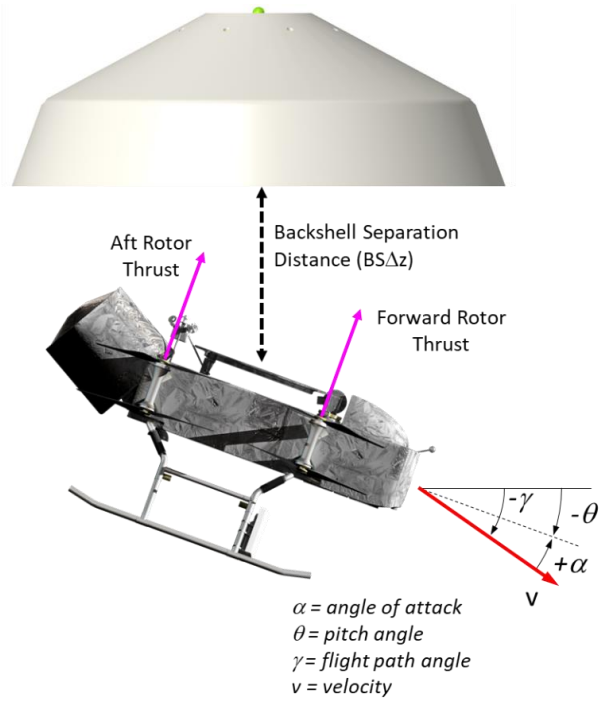

Figure 4. Dragonfly Lander Attitude and Rotor Angle of Attack Definition [19]

BACKSHELL RELEASE AND TRANSITION TO POWERED FLIGHT

Following the release of Dragonfly and its approximate one second free-fall to create positive separation from the backshell and parachute, the lander will spin up the rotors and start the pitch forward maneuver as shown in Fig. 3. Figure 5 below is reproduced from Wayne Johnson's work on rotor flow states in axial flow, and shows the boundaries achieved through the use of momentum theory for the various rotor flow states [20]. Note that this chart is for a perfectly vertical descent with zero forward speed. Additional information on the rotor flow states, specifically VRS which is a major focus of this paper, can be found in references [20-22]. Figure 5 makes use of a velocity scale parameter, v_h, which has been interpreted in this work as a hover equivalent induced inflow velocity based on the instantaneous rotor thrust. For a conventional helicopter, this parameter is nearly constant across most of the flight envelope. The TPF maneuver, however, assumes starting with the rotors lightly loaded and the scaling parameter close to zero, which places the rotor in the WBS. The y-axis represents the net flow through the rotor disk, i.e. the rotor axial speed, V_z, combined with the rotor induced velocity, v, normalized by v_h. The equivalent hover induced inflow velocity then increases as the rotors spin up and develop more thrust. This means that mapping the TPF maneuver onto the flow state chart would show a transition from WBS, up past TWS and VRS, and finally to a normal operating state.

A second TPF profile generated by an early Phase A

controller is used to show what this would really look like. The controller generated a time history of RPM and thrust values along the TPF curve that were needed for calculating v_h as described above. Figure 6 maps the output from this controller, which will be described in more detail in the next section, onto a similar non-dimensional aerodynamic chart with the various rotor flow states throughout the maneuver. Note the y-axis has been flipped as compared to Fig. 5, such that the rotor flow state tracks down and to the right similar to the lander along the TPF trajectory. The x-axis is now a forward speed ratio parameter that normalizes the rotor's edgewise speed, V_x, by v_h. The black line in the figure represents an approximate VRS stability boundary, indicating where VRS is typically encountered. The transition points between TWS and WBS have also been approximately labeled. The front and rear coaxial rotor pairs are shown to have different initial paths due to the varied RPMs required for the nominal pitch-down maneuver, but quickly align as steady-state flight is reached. The plot represents the first roughly nine seconds of the maneuver, indicating that a steady-state descent condition is arrived at quickly after initial release.

It is important to note this transition from WBS through TWS and VRS is unavoidable in the conventional mid-air deployment being discussed. Pitching forward more steeply, or quickly, will not preclude the rotors from crossing through the flow states, it only changes how long the rotors are in each flow state. The nominal trajectory can thus be optimized to successfully pass through these unsteady flow states as quickly as possible and emerge in the steady-descent forward-flight condition. The controller that created the nominal trajectory plotted in Fig. 6 will now be briefly discussed.

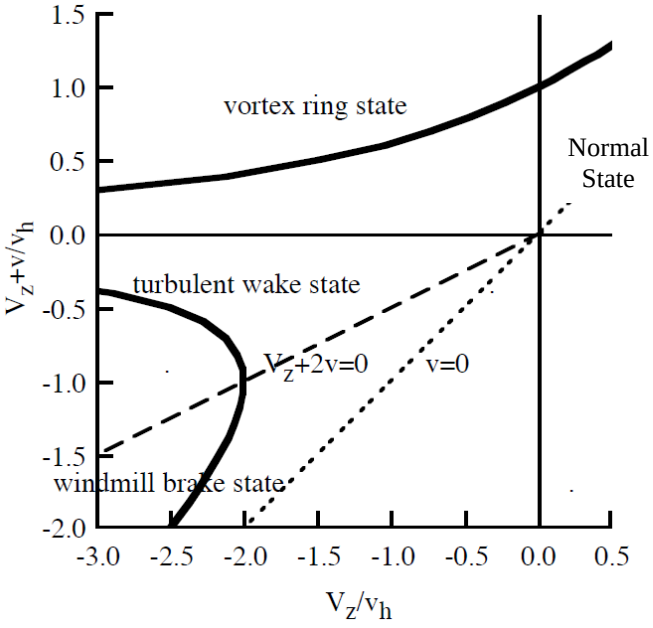

Figure 5. "Momentum theory and inflow states in axial flow," Reproduced from Ref. 20

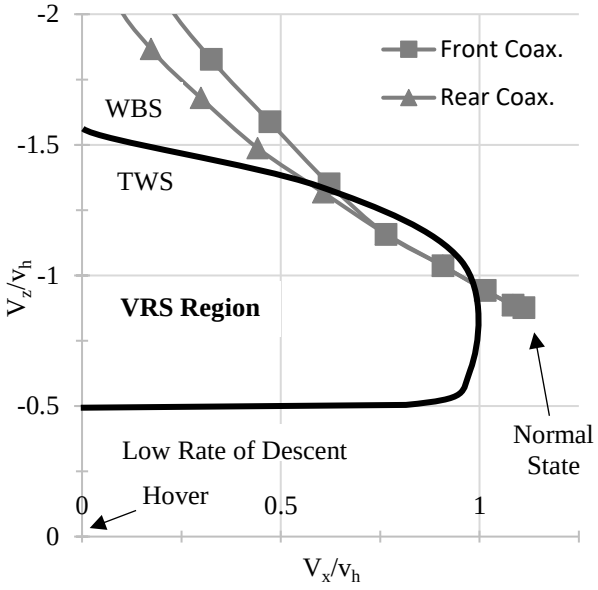

Figure 6. Rotor Flow States of the TPF Maneuver

TPF OPTIMAL TRAJECTORY AND CONTROLLER APPROACH

Dragonfly's flight on Titan from the controls perspective is based on the interaction of four components: the vehicle (airframe), the estimator (navigation filter), the flight controller, and the actuators. Each actuator consists of an electronic speed controller (ESC), a motor, and a rotor. The relationship between the four main components is shown in Fig. 7.

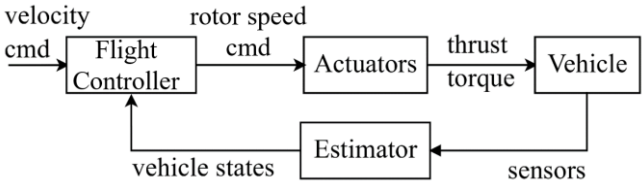

Figure 7. Dragonfly Control Architecture

For the flight controller discussed in this paper, which was developed by Opazo and Langelaan, the vehicle was assumed to be a rigid body subject to gravity, aerodynamic fuselage forces, and the thrust and torque generated by the rotors [23]. A brief high-level summary of the controller is presented here for better understanding of the TPF maneuver, but a more thorough description can be found in Ref. 23 that compares the specific controller with other control approaches. For the purpose of TPF commanded path generation, a longitudinal state model considering position, velocity, Euler angles, and angular rates was considered. The fuselage aerodynamic loads were calculated using results from previously created CFD tables and the estimator was assumed as ideal. The rotor itself is also a dynamic system where rotor speed is the result

of motor torque, aerodynamic torque, and rotor inertia. As such, the actuators are modeled using the three sub-components described earlier: an ESC, a brushless DC motor, and the rotor. This first order model is shown in Fig. 8.

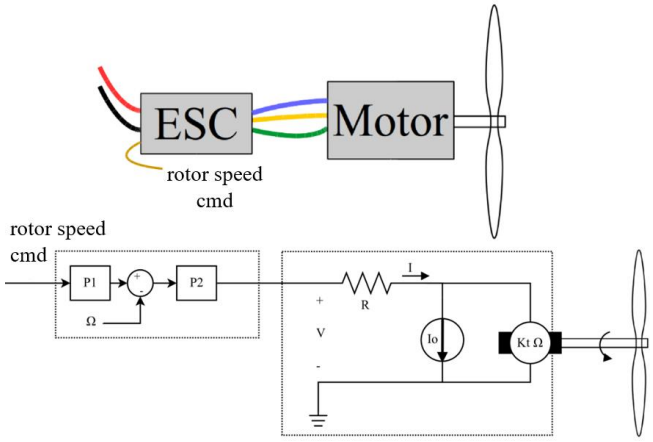

Figure 8. Motor, Rotor, and ESC System

The rotor thrust and torque values for a given speed and flight condition were calculated using a look-up performance table. The table included sweeps of angle of attack, flight speed, and rotor speed, and was generated with quasi-steady coaxial rotor CFD simulations. The flight controller, shown in Fig. 9, consists of on an external proportional-integral-derivate (PID) loop that receives a desired flight condition as input and outputs the necessary vehicle attitude. An inner PID loop then receives this vehicle attitude and outputs a rotor speed command for each motor.

The control approach for the TPF maneuver was done in a two-step process. An optimal trajectory was first calculated to safely transition between a nominal initial condition and the desired steady-state descent condition. Then a trajectory following controller was added to track that trajectory under both nominal and off-nominal release conditions. The optimal trajectory minimized the control effort and the deviation from the desired end state of the maneuver. The nominal initial condition refers to a terminal velocity and zero pendulum motion from the parachute-dragonfly pivot. Off nominal conditions are those where the lander is swinging under the parachute at lander release. A particle swarm optimization (PSO) was run on the PID controller gains in Fig. 9 to obtain a robust tracking of the optimal trajectory for nominal and a set of off-nominal initial conditions resulting in the final PSO flight controller. A TPF optimizer constraint criterion, J, was defined and measured as the maximum value of either velocity, pitch angle, or pitch-rate normalized by the maximum values as shown in Table 2. This corresponds to the minimum margin between the vehicle states and their respective maximum allowable values. Keeping a large margin from maximum limits, i.e. a low J value, is proposed as an indirect protection from undesirable aerodynamic rotor conditions.

Table 2. Optimizer Constraints

Variable	Value	Units
Pitch	45	[deg]
Pitch Rate	90	[deg/s]
Airspeed	12	[m/s]
Vertical Acceleration	3	[m/s^2]

Figure 10 displays the first seconds of the PSO controller's nominal trajectory. Various off-nominal release trajectories are also included and are colored by the resulting constraint criterion, where a J value of 1 represents an instantaneous violation of one or more of the design limits from Table 2.

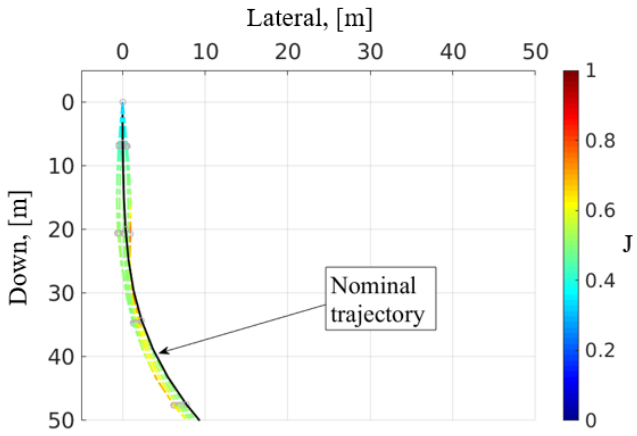

Figure 10. TPF Trajectory - Initial Release

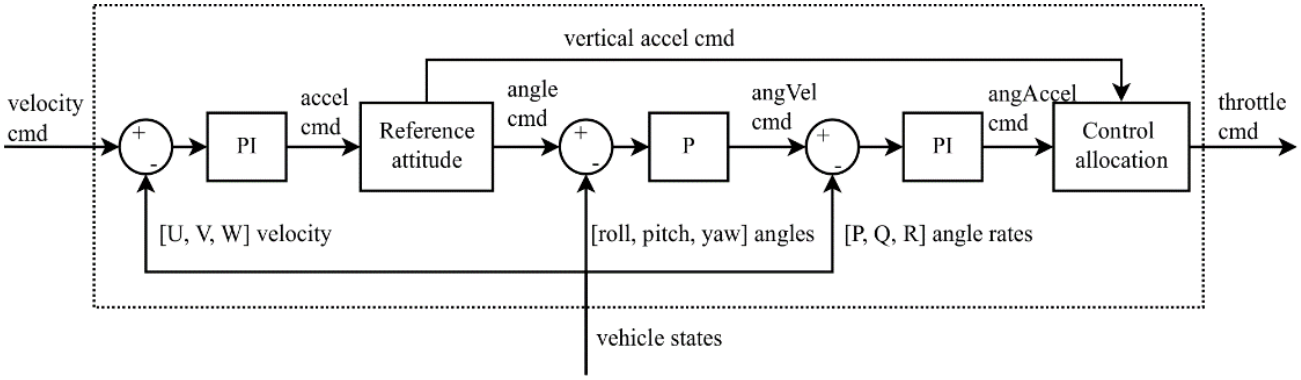

Figure 9. Early PSO Flight Controller

Figure 11 shows the full TPF maneuver ending with a steady-state descent that would be carried out to the landing location. The maximum and minimum constraint criterion results captured by the PSO controller are listed as J_{TPF} = 0.78 and 0.55, respectively. The minimum value is driven by the airspeed, which peaks around 6.25 m/s for the nominal trajectory. These J values represent having more than 20% margin from the design limits at all times.

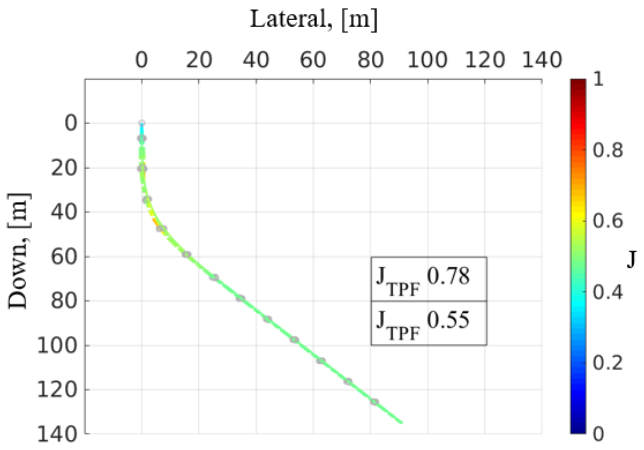

Figure 11. TPF Trajectory through Steady-state Descent

CFD SIMULATIONS OF TPF MANUEVER AND INTERACTIONAL AERODYNAMICS

A mid-fidelity CFD tool, called Rotorcraft CFD (RotCFD), has been used for fast engineering analyses of rotor performance and preliminary studies of the interactional aerodynamics between rotors, fuselage, and aeroshell. The tool uses a hybrid actuator disk and Unsteady Reynolds Averaged Navier Stokes (URANS) approach, which is shown in relation to other common methods in Fig. 12 as reproduced from Cornelius et al. [24].

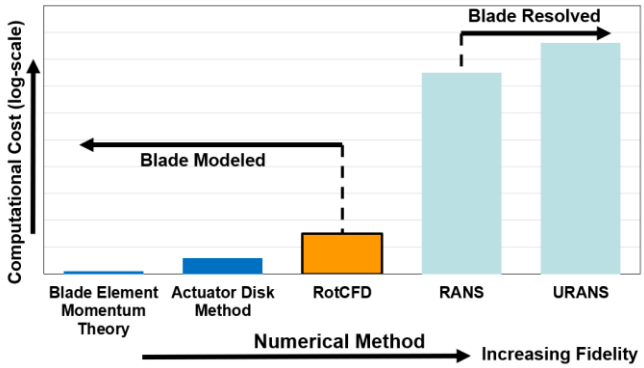

Figure 12. Computational Time vs. Model Fidelity for RotCFD Relative to Other Conventional Approaches [24]

The left side of Fig. 12 shows blade-modeled methods using simplifying assumptions for fast results, while the right side of the figure shows blade-resolved approaches that solve a form of the Navier-Stokes equations on the true blade geometry. The strictly blade-modeled methods deliver a lower level of fidelity that can have challenges in the flow states studied in this paper, while the blade-resolved methods require too great a computational cost with simulations taking on the order of days to weeks. RotCFD is depicted in the middle as having a low computational cost with accuracy suitable for engineering design by modeling the rotors within a CFD resolved flow-field. The tool captures relevant aspects of the rotor system such as hub and fuselage effects, rotor-rotor interactions, and the full rotor inflow and wake. Key information regarding the tool and prior verification efforts are provided in the reference section [25-33]. Of special interest are the recent studies into analyzing coaxial rotor systems using RotCFD [30-32] and the tool's performance on GPU accelerated machines [33].

For the simulations that incorporate the lander geometry along with the rotors, a C81 airfoil table input deck is used following the methods described by Koning et al. [34]. The airfoil tables presented in this paper were generated during Phase A using MIT-XFOIL [35]. Best practices have since been developed using the two-dimensional thin-layer Reynolds Averaged Navier-Stokes CFD solver, ARC2D [36]. These best practices combine methods from Koning, Critzos et al., Viterna and Corrigan, and Tangler and Kocurek [37-40]. The approach uses the CFD obtained results in the airfoil's attached flow regime, experimental NACA 0012 data in the separated flow regime, and the Viterna Corrigan correction to blend between the two.

Since the start of TPF occurs while the lander is still attached to the backshell, a preliminary study of the interactional aerodynamics of the lander and aeroshell system under a terminal velocity steady-state parachute descent was carried out. Figure 13 depicts the Dragonfly lander in its spacecraft configuration and within the aeroshell during atmospheric entry [9]. A simplified geometry for the aeroshell was created to capture the bluff-body aerodynamics and interactional effects to the lander under parachute descent pre- vehicle release. Figure 14 contains flowfield visualizations of local velocity around the aeroshell before and immediately following heatshield separation in a steady 3 m/s steady descent. The simulations suggest a benign separation with the lander shielded from jarring flow conditions during heatshield jettison.

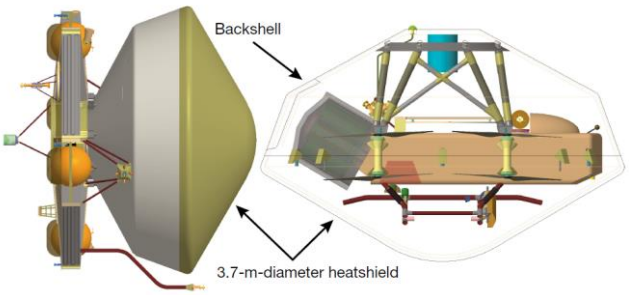

Figure 13. Dragonfly in Aeroshell, Picture Courtesy of Dragonfly/JHUAPL [9]

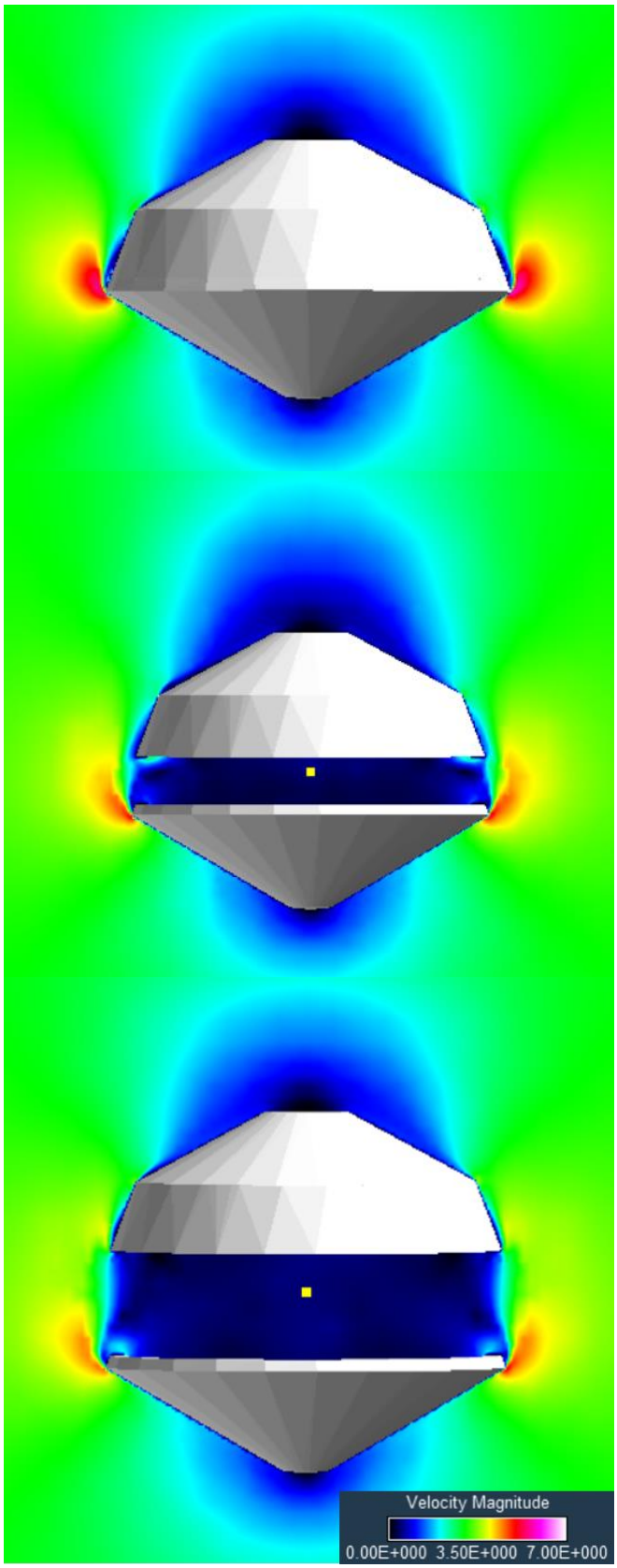

Figure 14. Aeroshell Flowfield Visualizations of Heatshield Deployment (Top to Bottom: 0 m, 0.5 m, 1 m)

After the heatshield has been jettisoned, the bottom of the lander and its rotors will be subjected to the impinging flow. Simulations were run with the lander still tucked in the backshell, as well as immediately after lander release at the start of the TPF sequence. Figure 15 depicts the Dragonfly Phase A CAD geometry used for the results presented in this paper.

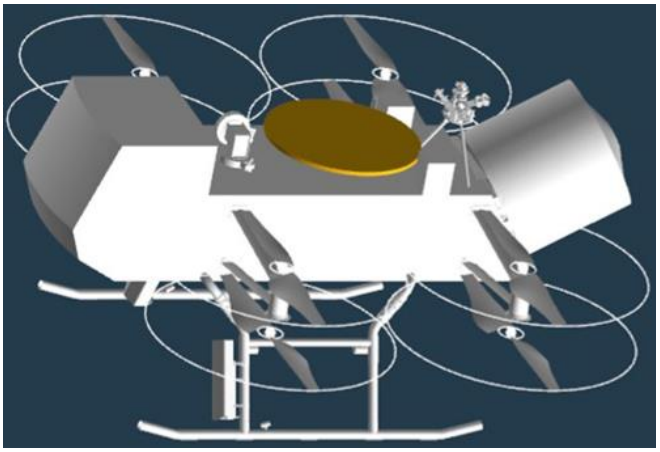

Figure 15. Dragonfly Phase A CAD Geometry

Figures 16-20 show a notional release sequence for the Dragonfly lander from the backshell. The simulations attempt to characterize the interactional aerodynamics pre- and post-release. Figure 16 is pre-release and shows that the flow field coming up through the rotors while still attached to the lander is slow due to the presence of the backshell. This case is of particular interest as too high of an upward flow through the rotors creates back-torque on the rotors working to spin them in the opposite direction. The TPF maneuver then starts with the free-fall release (delay) to create positive separation from the backshell and parachute and is shown in Fig. 17 with the lander translated 0.5 m away from the backshell. After roughly a one second free-fall, the rotors are commanded to continue spinning up and they quickly traverse the rotor flow state path described in Figures 5 and 6. When the lander is first released, the rotors are in the WBS flow condition (Fig. 17). As rotor speed is further increased and additional thrust develops on the rotors, they cross through the TWS (Figures 18-19) and then into VRS (Fig. 20). Figure 19 uses seeded particles to identify the streamlines and recirculating flow near the rotors and above the backshell in the TWS flow condition. The vector flowfields can also be observed to exhibit this recirculatory behavior that is especially apparent in VRS (Fig. 20) where a large-scale toroidal wake structure can be observed just beneath the plane of the rotors.

These figures loosely correspond to the TPF points zero, one, and two from the notional TPF profile in Fig. 3. The VRS condition exhibited in Fig. 20 is typically associated with a reduction in rotor thrust and a negatively damped state that pushes the rotor deeper into the condition. One could theoretically climb out of VRS with enough onboard power, but the easier approach to maintain positive separation from

the parachute and backshell is the pitch-forward maneuver to increase rotor advance ratio, emerge successfully from VRS, and continue to track the TPF profile. The rotor flow states from this scenario will now be studied more closely.

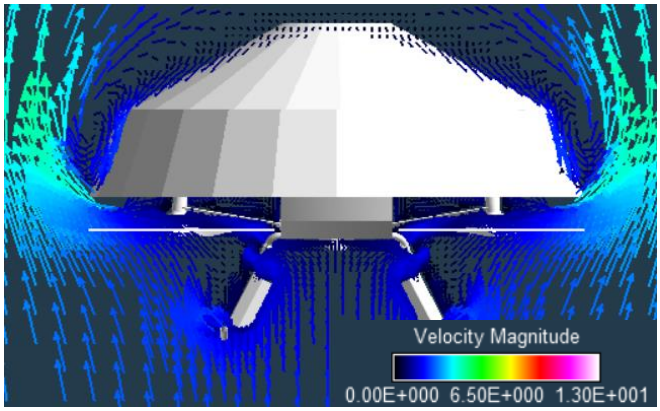

Figure 16. Backshell Release ~Pt. 0-, z = 0m, RPM = ~0, WBS

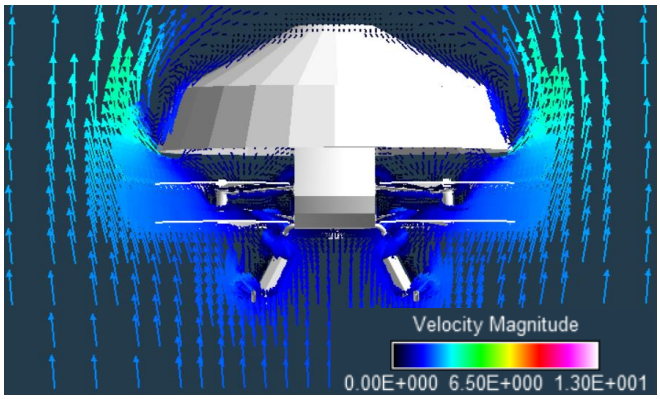

Figure 17. Backshell Release ~Pt. 1, z = 0.5m, RPM = ~0, WBS

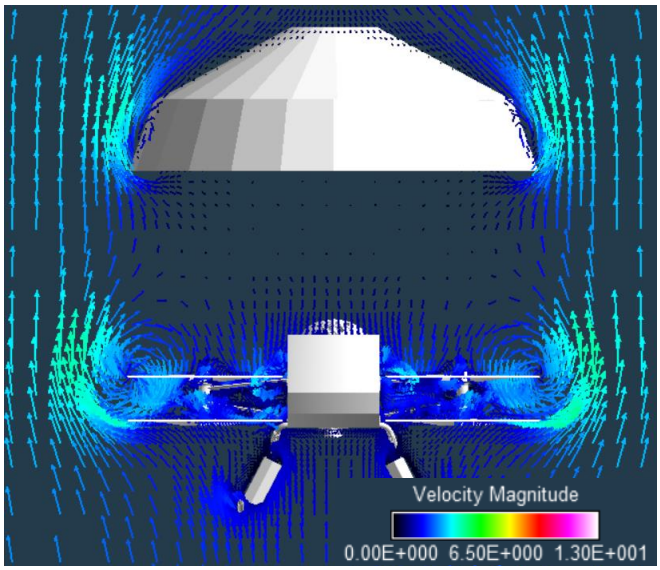

Figure 18. Backshell Release ~Pt. 1+, z = 2m, RPM = 410, TWS

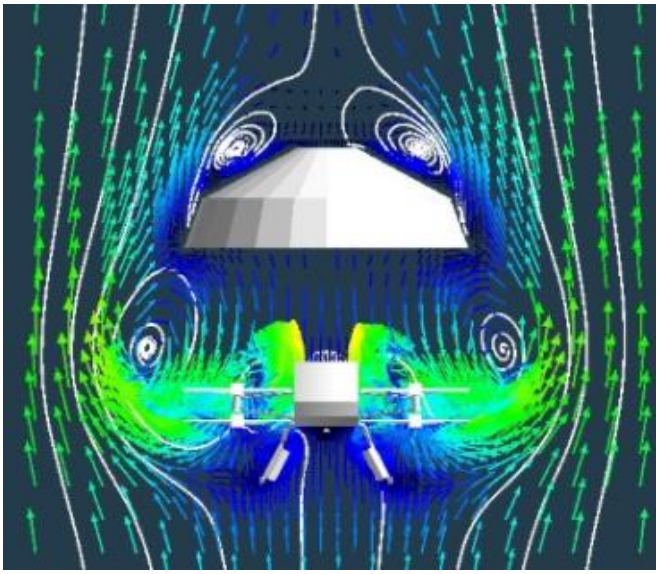

Figure 19. Backshell Release ~Pt. 1+, z = 2m, RPM = 410, TWS (Streamlines Added)

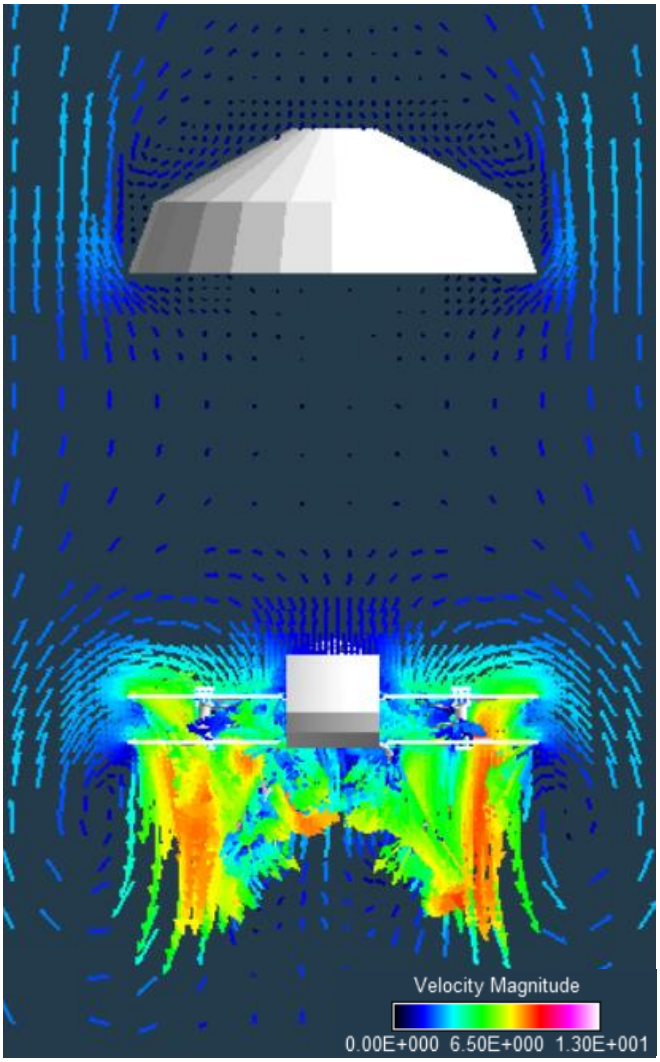

Figure 20. Backshell Release ~Pt. 2, z = 4m, RPM = 820, VRS

The flowfield around the lander is shown in Fig. 21 for several points along the notional TPF profile. These CFD analyses were carried out with the notional profile from Fig. 3 since it was used in previous work before the PSO controller profile was created. Separated flow can be viewed on the lander in various locations across the TPF maneuver and work has been carried out since Phase A to better streamline the fuselage. The TPF maneuver concludes when steady-state descent is successfully attained, corresponding to a lander pitch attitude close to zero for the PSO controller's nominal profile. This suggests that there would still be a few additional points required after point seven on the notional profile before the steady-state descent condition is reached. By comparing the notional profile to the PSO controller constraints, it is observed that the PSO approach restricts the lander pitch attitude more than the notional profile, which is thought to be helpful in preventing a runaway condition. It is worth noting, however, that the lander's terminal velocity in a nose dive is only on the order of 20 m/s in the thick Titan atmosphere.

These simulations were carried out using the notional profile to gain an understanding for the rotor flow states as well as thrust and power production versus location along the TPF trajectory. The simulations used a constant RPM of 600 in order to better isolate the effects of the various rotor flow states on the thrust and power with RPM held constant. Figures 22-23 map the rotor thrust and power versus TPF point number for simulations with the rotors only, i.e. first without fuselage. The first letter in the legend's naming convention defines front (F) or back (B), the second defines right (R) or left (L), and the third defines upper (U) or lower (L). The dashed blue line with squares, for example, represents the front-right lower rotor.

The rotor thrust appears to be highly variable between points zero through two in the maneuver as the rotors independently make their way through the various flow states from Fig. 6. Since these simulations were run at a constant RPM of 600, the WBS is likely not represented in the charts since the rotor thrust is already high even at point 0. This combination of rotor RPM and descent velocities from Fig. 3 likely puts the rotors initially in TWS or VRS and then to a normal operating state as the pitch-down maneuver is carried out. The variability is attributed to the various rotor-rotor interactions and the unsteadiness of TWS and VRS. Points three through seven see the thrust stabilize and separate into three distinct groupings from highest thrust to lowest thrust of front rotors, back upper rotors, and back lower rotors. The power comparisons show a strong dependence on the rotor induced power, which is a function of rotor thrust, but also see some variation attributed to the interaction of the various rotor wakes. An important takeaway is that the grouping of rotor power is tight, where-as the individual rotor thrust can vary greatly within the unsteady flow states and interactional rotor aerodynamics. This highlights the need for the optimizer constraints during the TPF maneuver as discussed with the PSO controller to avoid the high wake shadowing observed to decrease the back upper and lower rotor thrusts.

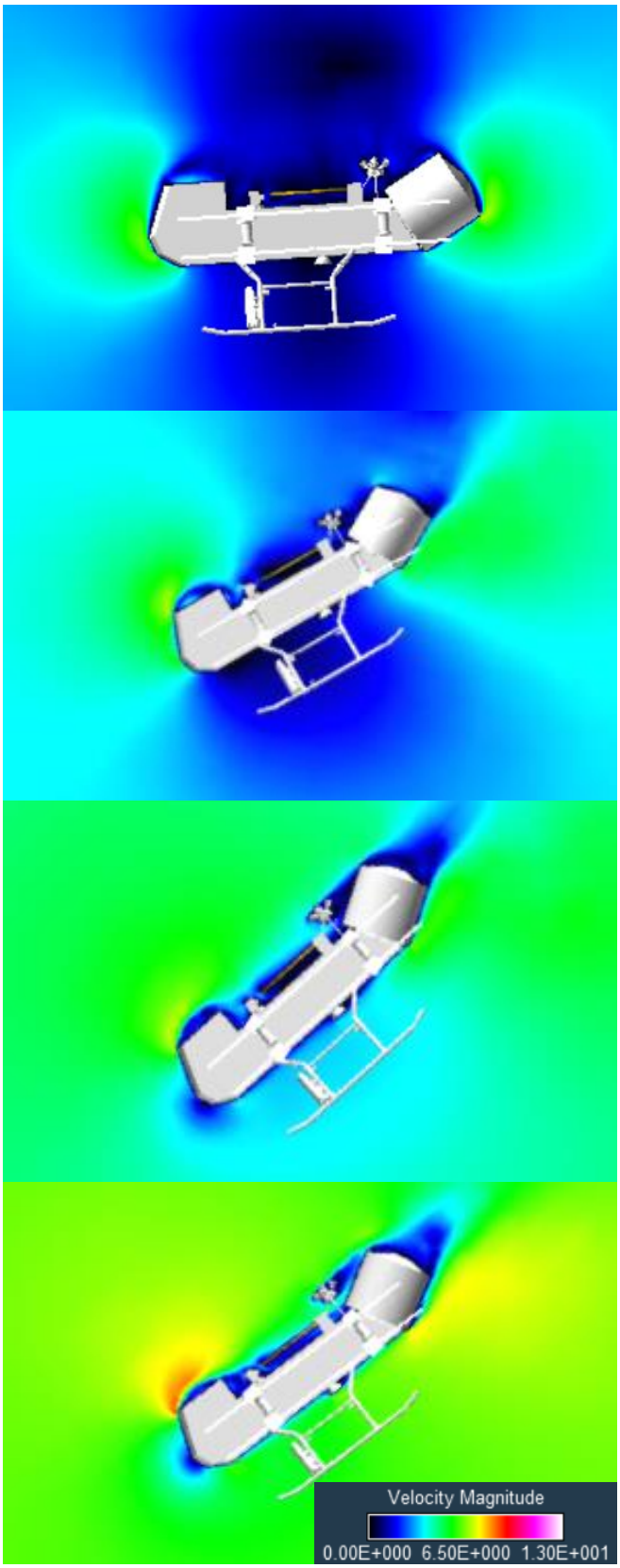

Figure 21. Notional TPF Profile Flow Visualizations Pts. 1, 3, 5, and 7, RPM = 600 (see Fig. 3)

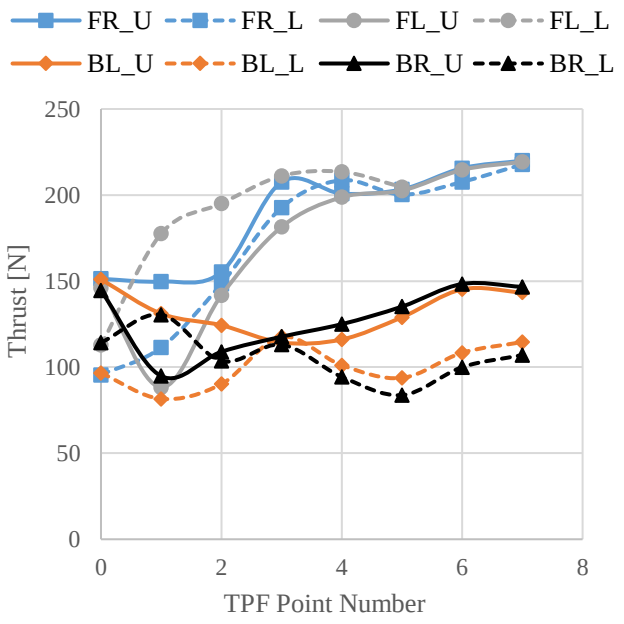

Figure 22. Rotors Only, Fig. 3 Profile, Thrust

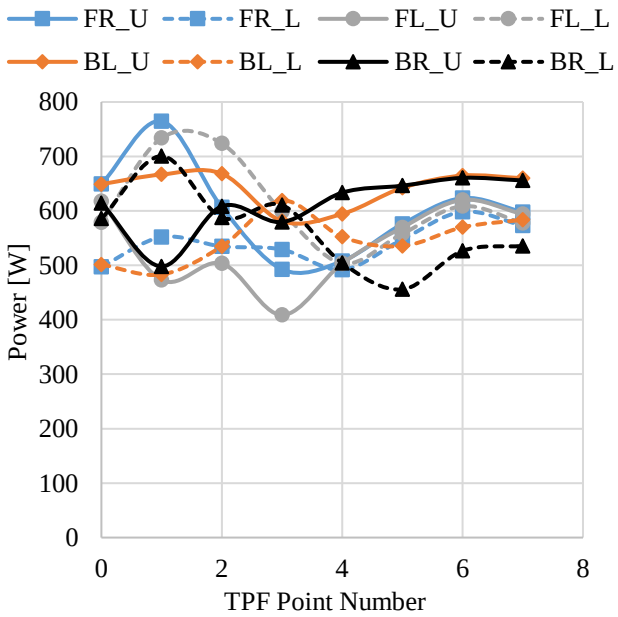

Figure 23. Rotors Only, Fig. 3 Profile, Power

Figures 24-25 show the same information for the simulations with the Dragonfly Phase A CAD geometry from Fig. 15 included. General observations are the same with slightly more variability due to rotor-fuselage interactions in addition to the previously mentioned rotor-rotor interactions. The total thrust seems to be higher for these simulations as compared to the rotors only, which could be due to the increased blockage of the fuselage in descent working to change the velocity near the rotors.

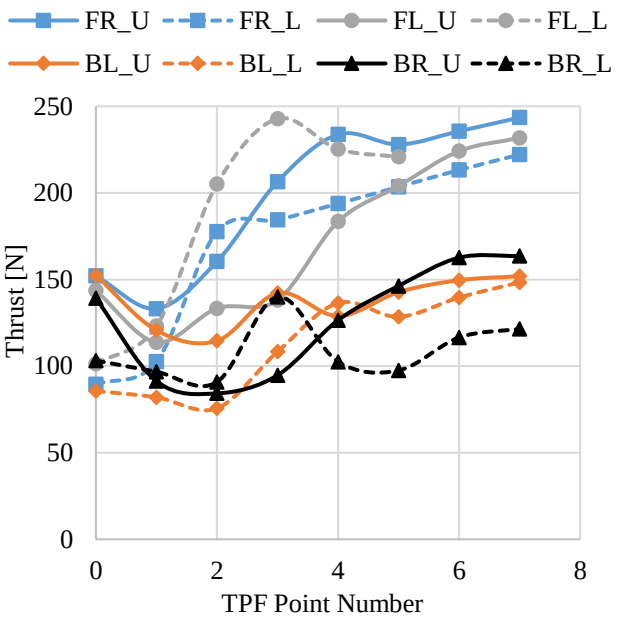

Figure 24. Full Lander, Fig. 3 Profile, Thrust

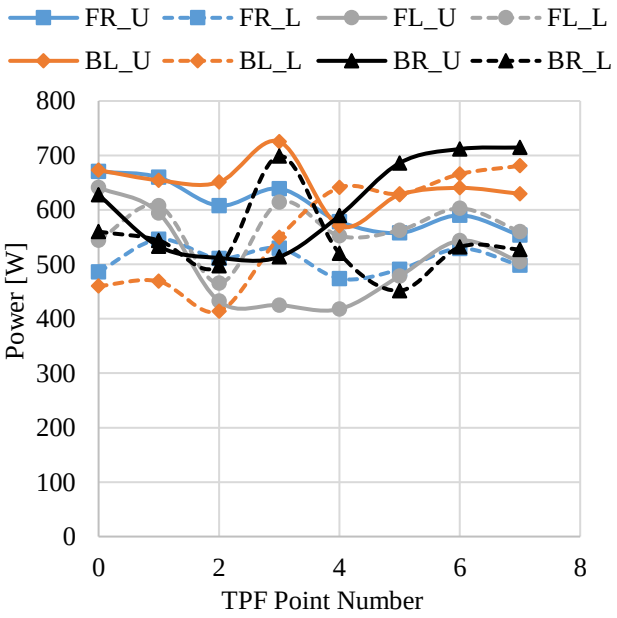

Figure 25. Full Lander, Fig. 3 Profile, Power

CFD SIMULATIONS OF STEADY AXIAL DESCENT

Simulations of the lander were also carried out in axial descent to develop a better understanding of the interactional aerodynamic effects in the early stages of the TPF maneuver and in axial descent in general. Figures 26 and 27 show side and front views of the lander in a 2.5 m/s steady descent with total thrust approximately balancing lander weight and drag. The velocity flowfied in the plane of the rotors from the front view (Fig. 27, top) shows that the rotors still have a high inflow down through them suggesting a normal operating

state. The dark blue areas beneath the lander and off the blade tips, however, suggest the proximity to VRS. Figure 27 (bottom) uses velocity vectors to highlight this large-scale toroidal wake structure beneath the lander.

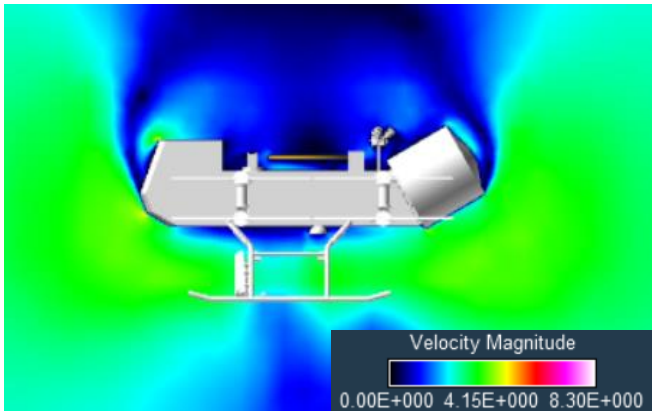

Figure 26. Steady Axial Descent Side View, Velocity = 2.5 m/s, RPM = 600

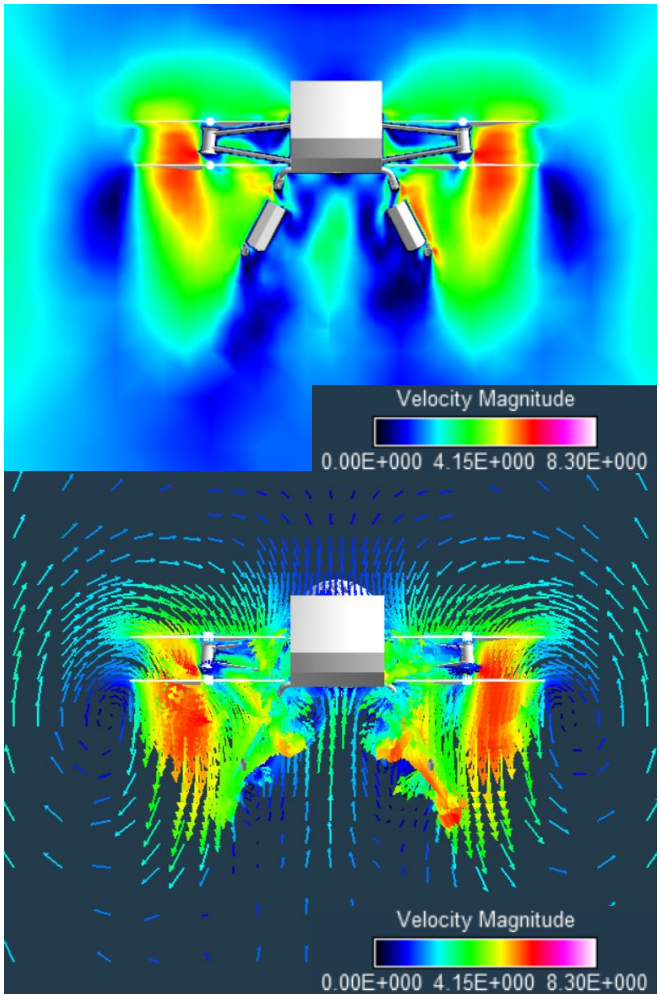

Figure 27. Steady Axial Descent Front View, Velocity Visualizations of VRS, Velocity = 2.5 m/s, RPM = 600

Figure 28 illustrates the lander's total rotor thrust, i.e. all eight rotors added together, as a function of steady axial descent speeds for the Dragonfly geometry at a constant RPM. A slight thrust decrease can be observed early on around the VRS region before the thrust rapidly increases again with increasing inflow from beneath the rotors. The very small dip in thrust is consistent with the observations made by Kinzel et al. for coaxial rotor systems in axial descent in and around VRS [41]. The findings suggest that a coaxial rotor system sees less thrust loss in and around VRS than an equivalent solidity single rotor operating at the same hover thrust coefficient. The coaxial system's lower rotor sees the high thrust loss normally associated with the beginning of VRS and flow visualizations show the toroidal vortex ring in proximity to the lower rotor. The upper rotor maintains high thrust and remains separated from the vortex ring until a higher descent rate. Figure 29 is the corresponding plot for total rotor power across the lander and confirms the changing rotor flow states from normal operation in hover (0 m/s), to a zero-power condition around 9 m/s for the 600 RPM descent cases, and finally to negative power within WBS. Figure 30 maps this steady axial descent sweep onto the same rotor aerodynamic chart from Fig. 6. Since the cases are in axial descent, the points lie on the y-axis. The results show a transition from hover, up through the VRS region, past TWS, and finally into WBS. Note that this is the opposite progression as compared to Fig. 6 since the rotors here started at a high disk-loading, i.e. high v_h, and zero descent velocity. The flow state tracked upward along the plot as the descent speed was increased, increasing the flow upward through the rotors until ending in WBS.

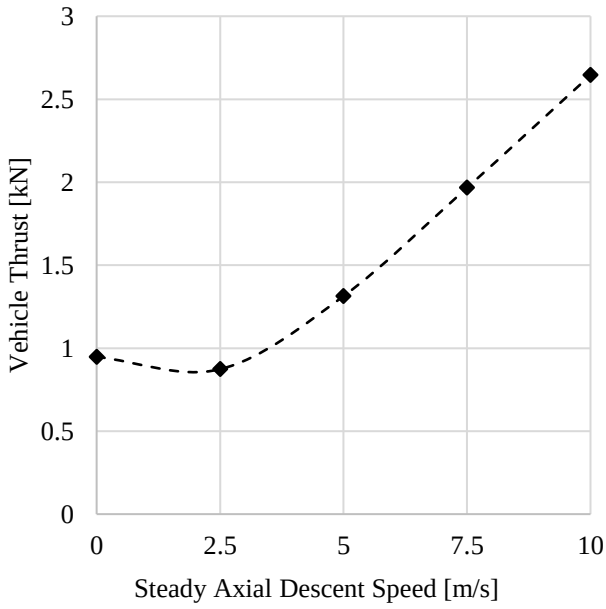

Figure 28. Steady Axial Descent, Lander Total Thrust, RPM = 600

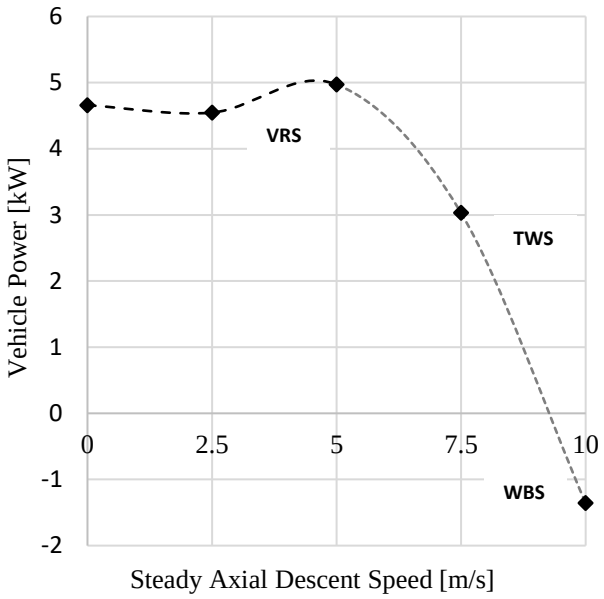

Figure 29. Steady Axial Descent, Lander Total Power, RPM = 600

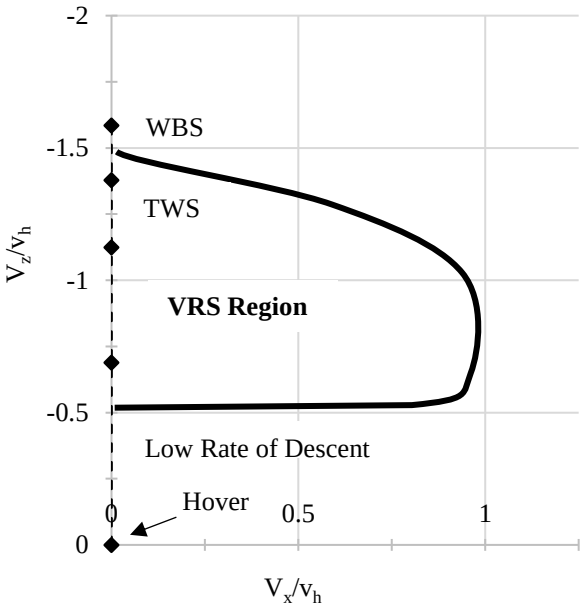

Figure 30. Steady Axial Descent, Rotor Flow State Chart, RPM = 600

CONCLUSIONS

This paper presents a preliminary study into the transition to powered flight (TPF) maneuver of the Dragonfly lander currently under development to fly on Saturn's largest moon, Titan, in the 2030s. TPF is a mid-air deployment starting under parachute descent following atmospheric entry and concludes when a steady-state descent condition is achieved. The idea behind TPF was first introduced and then followed by a discussion of the various rotor aerodynamic flow states associated with the maneuver. Mapping the TPF profile onto a rotor aerodynamic state chart showed how the rotors start in the windmill break state (WBS), successfully pass through the turbulent wake state (TWS) and the vortex ring state (VRS), and finally reach a normal operating state. It was explained that this progression through the rotor flow states is unavoidable for the conventional mid-air deployment presented, but that controller optimization can be used to reduce the amount of time in unsteady flow conditions.

A high-level discussion detailed one of the control approaches used in Phase A of the program. The controller approach based on particle swarm optimization was introduced in order to find and track a pre-determined nominal trajectory from both nominal and off-nominal parachute release conditions. Lander attitude and rate constraints were used in the controller design to avoid unfavorable rotor aerodynamic situations, and a constraint criterion was used to assess the effectiveness of the controller. This optimal trajectory was then mapped onto the rotor aerodynamic flow state chart and showed the successful progression of the rotor flow states throughout the TPF maneuver to a steady-state descent condition.

Preliminary CFD analyses were presented for the following Phase A Dragonfly lander configurations:

1. Aeroshell only (backshell and heatshield release)
2. Backshell and Dragonfly lander release
3. Dragonfly along notional TPF profile
4. Dragonfly in quasi-steady axial descent

The results of the aeroshell stimulations suggest the flow state around the heatshield release process is benign and that the flow up through the rotors is not sufficient enough to start them spinning in the opposite direction. Further studies should be carried out to verify these preliminary findings and the minimum required aerodynamic torque to start the rotor and motor pair spinning. The CFD simulations of the Dragonfly lander along the notional TPF profile confirm the theoretical description of the TPF maneuver and the rotor flow state transition from WBS, through TWS and VRS, and finally to a normal operating state. The thrust and power across the eight rotors were observed to be variable in the first seconds of the maneuver. This suggests that a flight test experiment of the mid-air deployment with rotors initially at rest, or at least lightly loaded, would be helpful for the controller testing. The closed loop nature of the controller would likely be adequate to compensate for the unsteady thrust and accomplish the desired pitch-down maneuver. The rotor flow state, and thus thrust and power, quickly reach a stable condition after the pitch-down maneuver is carried out and an adequate advance ratio is attained to clear the rotor wakes and successfully emerge out of VRS. This entire transition occurs within the first several seconds of the TPF maneuver. Further simulations of the lander in axial descent showed the trends of total rotor thrust and power at constant RPM. The results agree with past findings showing a coaxial

rotor shielding phenomenon of the upper rotor by the lower rotor in proximity to VRS, which results in less thrust loss as compared to a single rotor with the same solidity and hover thrust coefficient. The phenomenon appears to maintain upper rotor thrust and delay the full effects of VRS to a higher descent rate.

Future work will build on the simulations presented to analyze the current Phase B Dragonfly configuration along the Phase B flight controller's nominal TPF trajectory. Additional studies will also likely explore the interactional aerodynamics of the lander in the backshell and in axial descent, specifically with respect to aerodynamic and vibratory loads of coaxial rotor systems in and around VRS.

Author contact: Jason K. Cornelius joc5693@psu.edu

ACKNOWLEDGMENTS

This research effort is funded through the National Science Foundation Graduate Research Fellowship Program and the NASA New Frontiers Program. The authors would like to extend their gratitude to William Polzin of Sukra Helitek Incorporated for his continued support as well as the late Dr. Ganesh Rajagopalan for his support of the project and his contributions to enable increased access to CFD analysis methods used in this paper. Additionally, the authors would like to thank Witold Koning, Dr. Natasha Schatzman, and Dr. William Warmbrodt of the NASA Ames Research Center for their support and guidance of this work.

REFERENCES

1. Lorenz, R., "Saturn's Moon Titan; from 4.5 billion years ago to the present," Owner's Workshop Manual, Haynes Publishing, 2020. ISBN13: 9781785216435
2. Young, L. A., Chen, R. T. N., Aiken, E. W., Briggs, G. A., "Design Opportunities and Challenges in the Development of Vertical Lift Planetary Aerial Vehicles," Proceedings of the American Helicopter Society International Vertical Lift Aircraft Design Specialist's Meeting, January 2000.
3. Young, L. A., "Vertical Lift - Not Just for Terrestrial Flight," Proceedings of the AHS/AIAA/RaeS/SAE International Powered Lift Conference, Arlington, VA, October 30- November 1, 2000.
4. Lorenz, R. D., "Post-Cassini exploration of Titan: Science rationale and mission concepts," Journal British Interplanetary Society, Vol. 53 No. 7/8, 2000, pp. 218-234.
5. Lorenz, R. D., "Flexibility for Titan Exploration: The Titan Helicopter," Forum on Innovative Approaches to Outer Planetary Exploration 2001–2020, Feb. 2001.
6. Young, L. A., "Exploration of Titan Using Vertical Lift Aerial Vehicles," Forum on Innovative Approaches to Outer Planetary Exploration 2001–2020, Feb. 2001.
7. Lorenz, R. D., "Flight power scaling of airplanes, airships, and helicopters: Application to planetary exploration," Journal of Aircraft, Vol. 38 No. 2, pp 208-214, 2001. https://doi.org/10.2514/2.2769
8. Lorenz, R. D., "The Exploration of Titan," Johns Hopkins APL Technical Digest, Vol. 27 No. 2, pp. 133–144, 2006.
9. R. D. Lorenz, E. P. Turtle, J. W. Barnes, M. G. Trainer, D. S. Adams, K. E. Hibbard, C. Z. Sheldon, K. Zacny, P. N. Peplowski, D. J. Lawrence, M. A. Ravine, T. G. McGee, K. S. Sotzen, S. M. MacKenzie, J. W. Langelaan, S. Schmitz, L. S. Wolfarth, and P. Bedini, "Dragonfly: A Rotorcraft Lander Concept for Scientific Exploration at Titan," Johns Hopkins Technical Digest, Vol. 34 No. 3, pp. 374–387, 2018.
10. Langelaan, J., Schmitz, S., Palacios, J., and Lorenz, R., "Energetics of rotary-wing exploration of titan," IEEE Aerospace Conference, Big Sky, Montana, 2017.
11. Grip, H., Johnson, W., Malpica, C., Scharf, D., Mandic, M., Young, L., Allan, B., Mettler, B., Martin, M., Lam, J., "Modeling and Identification of Hover Flight Dynamics for NASA's Mars Helicopter," AIAA Journal of Guidance, Control, and Dynamics, Vol. 43, No.2, Feb. 2020. https://doi.org/10.2514/1.G004228
12. Balaram, J., Canham, T., Duncan, C., Golombek, M., Grip, H., Johnson, W., Maki, J., Quon, A., Stern, R., Zhu, D., "Mars Helicopter Technology Demonstrator," AIAA SciTech Forum, Kissimmee, Florida, 2018.
13. Young, L. A., and Aiken, E. W., "Vertical Lift Planetary Aerial Vehicles: Three Planetary Bodies and Four Conceptual Design Cases," Presented at 27th European Rotorcraft Forum, Moscow, Russia, September 11-14, 2001.
14. Young, L.A., "Exploration of Titan Using Vertical Lift Aerial Vehicles," NASA Headquarters and Lunar and Planetary Institute Forum on Innovative Approaches to Outer Planetary Exploration, LPI Contribution # 1084, Houston, TX, February 21-22, 2001.
15. Young, L. A., Aiken, E. W., Derby, M. R., Johnson, J. L., Navarrete, J., Klem, J., Demblewski, R., Andrews, J. and Torres, R. "Engineering Studies into Vertical Lift Planetary Aerial Vehicles," Presented at the AHS International Meeting on Advanced Rotorcraft Technology and Life Saving Activities, Tochigi, Japan, November 2002.
16. Young, L.A., Pisanich, G., and Ippolito, C., "Aerial Explorers," 43rd AIAA Aerospace Sciences Meeting, Reno, NV, January 10-13, 2005.
17. Barnes, J., Lemke, L., Foch, R., McKay, C., Beyer, R., Radebaugh, J., Atkinson, D., Lorenz, R., Le Mouelic, S., Rodriguez, S., Bain, S., Kattenhorn, S., Colaprete, A., "AVIATR – Aerial Vehicle for In-Situ and Airborne Titan Reconnaissance," Experimental Astronomy, Vol. 33 No. 1, pp. 55–127 (2012). https://doi.org/10.1007/s10686-011-9275-9
18. Stofan, E., Lorenz, R., Lunine, J., Bierhaus, E., Clark, B., Mahaffy, P., Ravine, M., "TiME—The Titan Mare Explorer," IEEE Aerospace Conference, Big Sky, MT, paper 2434, 2013.
19. Hibbard, K., Adams, D., Lorenz, R., Turtle, E., Bedini, P., Langelaan, J., "Dragonfly: Rotorcraft Landing on

Titan," 15th International Planetary Probe Workshop, June 2017.
20. Johnson, W., "Model for Vortex Ring State Influence on Rotorcraft Flight Dynamics," NASA/TP-2005-213477, published online 1 Dec. 2005. https://ntrs.nasa.gov/citations/20060024029
21. Leishman, J. G., Bhagwat, M. J., Ananthan, S., "The Vortex Ring State as a Spatially and Temporally Developing Wake Instability," Journal of the American Helicopter Society, Vol. 49, No. 2, April 2004, pp. 160-175. https://doi.org/10.4050/JAHS.56.022001
22. Brand, A., Dreier, M., Kisor, R., Wood, T., "The Nature of Vortex Ring State," Journal of the American Helicopter Society, Vol. 56, No. 2, April 2011. https://doi.org/10.4050/JAHS.56.022001
23. Opazo, T., and Langelaan, J., "Longitudinal control of transition to powered flight for a parachute dropped multi-copter," AIAA SciTech Forum, AIAA 2020-2072.
24. Cornelius, J., Schmitz, S., Kinzel, M., "Efficient Computational Fluid Dynamics Approach for Coaxial Rotor Simulations in Hover," Journal of Aircraft, Vol. 58 No. 1, Jan. 2021. https://doi.org/10.2514/1.C036037
25. Sukra Helitek, RotCFD: Rotor Computational Fluid Dynamics Integrated Design Environment, Software Package, Ver. 0.9.15 Build 402, Ames, IA, 2020. http://sukra-helitek.com/
26. Rajagopalan, G., Baskaran, V., Hollingsworth, A., Lestari, A., Garrick., D., Solis, E., and Hagerty, B., "RotCFD – A Tool for Aerodynamic Interference of Rotors: Validation and Capabilities," AHS Future Vertical Lift Aircraft Design Conference, San Francisco CA, Jan. 2012. https://rotorcraft.arc.nasa.gov/Publications/files/A-5-D_rajagopalan.pdf
27. Patankar, S. V., *Numerical Heat Transfer and Fluid Flow*, Hemisphere Publishing Corp, New York, 1980.
28. Favre, A. J., "The Equations of Compressible Turbulent Gases," Report AD0622097, Aix-Marseille Univ., Inst. De Mecanique Statistique de la Turbulence, Marseille, France, Jan. 1965. https://apps.dtic.mil/sti/citations/AD0622097
29. Karki, K. C., and Patankar, S. V., "Pressure-based calculation procedure for viscous flows at all speeds in arbitrary configurations," AIAA Journal, Vol. 27, No. 9, Sept. 1989. https://doi.org/10.2514/3.10242
30. Schatzman, N., "Aerodynamics and Aeroacoustic Sources of a Coaxial Rotor," NASA/TM-2018-219895, Nov. 2018. https://ntrs.nasa.gov/citations/20180003216
31. Cornelius, J., Kinzel, M., Schmitz, S., "Efficient CFD Approaches for Coaxial Rotor Simulations," AIAA SciTech 2019 Forum, AIAA 2019-1658. https://doi.org/10.2514/6.2019-1658
32. Conley S, Russell C, Kallstrom K, Koning W, Romander E., "Comparing RotCFD Predictions of the Multirotor Test Bed with Experimental Results," VFS Forum 76, Oct. 2020.
33. Rajagopalan, G., Thistle, J., and Polzin, W., "The Potential of GPU Computing for Design in RotCFD," AHS Technical Meeting on Aeromechanics Design for Transformative Vertical Lift, San Francisco, CA, Jan. 2018. https://rotorcraft.arc.nasa.gov/Publications/files/Rajagopalan_2018_TechMx.pdf
34. Koning, W., Johnson, W., and Grip, H., "Improved Mars Helicopter Aerodynamic Rotor Model for Comprehensive Analyses," AIAA Journal, Vol. 57, No. 9, Sept. 2019. https://doi.org/10.2514/1.J058045
35. Drela, M., "XFOIL: An Analysis and Design System for Low Reynolds Number Airfoils," Low Reynolds Number Aerodynamics, Springer, Berlin, Heidelberg, 1989, pp 1-12.
36. ARC2D NASA, ARC2D (Efficient Two-Dimensional Solution Methods for The Navier-Stokes Equations), Software Package, Build: July 2018, Mountain View, CA.
37. Koning, W., "Generation of Performance Model for the Aeolian Wind Tunnel (AWT) Rotor at Reduced Pressure," NASA/CR–2018–219737, published online Dec. 2018. https://ntrs.nasa.gov/citations/20180008699
38. Critzos, C., Heyson, H., and Boswinkle, R., "Aerodynamic Characteristics of NACA 0012 Airfoil Section at Angles of Attack From 0-180 Degrees," NACA TN-3361, Jan. 1955. https://ntrs.nasa.gov/citations/19930084501
39. Viterna, L., and Corrigan, R., "Fixed Pitch Rotor Performance of Large Horizontal Axis Wind Turbines," DOE/NASA Workshop on Large Horizontal Axis Wind Turbines, published online Jan. 1982. https://ntrs.nasa.gov/citations/19830010962
40. Tangler, J., and Kocurek, J., "Wind Turbine Post-Stall Airfoil Performance Characteristics Guidelines for Blade-Element Momentum Methods," 43rd AIAA Aerospace Sciences Meeting and Exhibit, AIAA-2005-591, Reno, NV, 2005. https://doi.org/10.2514/6.2005-591
41. Kinzel, M., Cornelius, J., Schmitz, S., Palacios, J., Langelaan, J., Adams, D., and Lorenz, R., "An Investigation of the Behavior of a Coaxial Rotor in Descent and Ground Effect," AIAA SciTech Forum, AIAA 2019-1098. https://doi.org/10.2514/6.2019-1098